Classifying land cover based on calibrated full-waveform airborne light detection and ranging data

Guangcai Xu (徐光彩), Yong Pang (庞 勇)*, Zengyuan Li (李增元), Dan Zhao (赵 旦), and Dan Li (李 丹)

Institute of Forest Resource and Information Technology, Chinese Academy of Forestry, Beijing 100091, China

**Corresponding author: caf.pang@gmail.com*

Received March 7, 2013; accepted May 13, 2013; posted online July 26, 2013

The capability of the parameters derived from waveform data in discriminating objects is assessed and the effect of the relative calibration of full-waveform data in discriminating land-cover classes is evaluated. Firstly, a non-linear least-squares method with the Levenberg–Marquardt algorithm is used to fit the return waveforms by a Gaussian function. Gaussian amplitude, standard deviation, and energy are extracted. Secondly, a relative calibration method using the range between the sensor and the target based on a radar equation is applied to calibrate amplitude and energy. The change in transmit pulse energy is also considered in this process. A support vector machine classifier is used to distinguish the study area into non-vegetated area (including roads, buildings, and vacant lots), grassland, needle-leaf forests, and broad-leaf forests. The overall classification accuracy ranges from 79.33% to 87.6%, with the combination of the two groups of the three studied parameters. Calibrated data classification accuracy is improved from 1.20% to 6.44%, thus resulting in better forest type discrimination. The result demonstrates that the parameters extracted from the waveforms can be applied effectively in identifying objects and that relative calibrated data can improve overall classification accuracy.

OCIS codes: 280.3640, 100.6890.

doi: 10.3788/COL201311.082801.

Small-footprint airborne LiDAR systems currently have two types. The first type is the traditional discrete LiDAR system which only provides 3D coordinates and intensity information. The second type is the full-waveform LiDAR system. Compared with traditional discrete LiDAR systems, full-waveform LiDAR systems digitize and record the entire backscattered signal of each emitted pulse as a function of time, thus providing more controls to end users for managing and interpreting raw data during post-processing.

Small-footprint airborne LiDAR data classification is primarily focused on distinguishing ground points from non-ground points. In this case, discriminating ground points is based on elevation information; hence, several filtering methods that employ altitude have been developed for obtaining accurate topographic data[1]. However, with the increasing demand on LiDAR applications, geometry-based filtering methods for acquiring terrain information are inadequate for meeting the requirements of non-ground point classification. By contrast, a number of researchers have analyzed geomorphological structure mine information from geometry data for classifying land cover. Feature extraction and object recognition/reconstruction methods have been introduced in LiDAR data processing. These methods include height texture measurements and a mathematical morphological approach for separating man-made and natural objects[2], a non-parametric technique of mean shift for the power line model[3], and an object-based analysis method for application in urban areas[4]. These studies have mainly focused on human settlements, but using these methods for subclassifying vegetation areas is difficult. By contrast, geometry from LiDAR data is often used to provide additional classification input or decision layer when combined with a multispectral or hyperspectral image[5−7]. However, the disadvantage of this technique is that the registration and scale conversion between LiDAR and optical data should also be considered.

The emergence of small-footprint full-waveform LiDAR provides a new capability for classifying land cover. Width, amplitude, and energy are the most important extra-physical properties from full-waveform data[8] that can be explored for identifying ground and vegetation point[8−10], deriving higher quality terrain models[11], and particularly, classifying tree species[12−16]. However, most studies combing geometry information may affect the assessment of the classification capability of the parameters derived from waveform data. Moreover, few studies consider full-waveform data calibration in classification.

LiDAR return echo is affected by numerous factors involving emission pulse frequency, divergence angle, pulse width, scan angle, atmosphere, flight speed, distance, terrain, etc. These factors must be eliminated to evaluate target radiation characteristics correctly. The influence of certain factors can be assumed as constant in a small area. Then, return waveforms can be simplified to reflect the reflective properties of the targets. However, lack of calibration makes these methods difficult to employ on a large scale because of the influence of widely varying factors. Therefore, calibrating received waveforms is necessary for object recognition and automatic classification.

A number of studies have attempted calibrating LiDAR data. By contrast, several scholars have conducted research on factors influencing calibration based on LiDAR mechanism, such as reviewing certain basic physical concepts used by the remote-sensing community[17], the specific influence of the calibrated results of data-

driven and model-driven methods, and the effect of incidence angles on buildings[18,19]. Meanwhile, a number of researchers have studied calibration methods through experiments, such as using bright natural targets or manmade objects with known reflectance to correct the return signal[20,21]. However, current LiDAR data calibration theory is not perfect, and a unified standard has not yet been developed.

The objectives of the present study are as follows: 1) to calibrate the Gaussian decomposition results of full-waveform data using the range and normalization of transmitted pulses; 2) to evaluate the capability of parameters derived from waveform data in discriminating objects without any geometry information; 3) to explore the effect of landscape identification after calibration.

The study area is located in the Lingshui National Nature Reserve, Yichun City, Heilongjiang Province. The center geographical coordinates are approximately 128° 53′ 20″ E and 47° 10′ 50″ N, with elevation ranging from 280 to 707 m above the mean sea level and a slope of less than 40°. More than 98% of this area is covered by forest. Land cover types include needle-leaf forest, grassland, and non-vegetated area (including roads, buildings, and vacant lots)

LiDAR data acquisition was conducted during the summer of 2009 at a leaf-on condition using the a scanner (LMS-Q560, Riegl, Austria) with a full-waveform digitizer. The waveform digitizer records both transmitted and backscattered pulses. Ten flight lines with approximately 80% overlap were designed to cover 1 600 ha of the center of the nature reserve. Data collection configuration results in a point density of approximately 3 points/m^2. The charge-coupled device (CCD) image consisting of three bands (red, green, and blue (RGB)) with a resolution of 20 cm was simultaneously acquired, geometrically corrected, and orthorectified based on a digital surface model.

A ground survey of 21 plots was conducted simultaneously, and more accurate data based on individual tree locations were collected from July 2010 through August 2010. The 21 sample plots were located via differential global positioning system (DGPS). Each tree in several typical plots, as well as 981 single trees were surveyed to acquire the precise position of each tree via DGPS and electronic total station. The average position error is 0.48 m, whereas the maximum error is 0.89 m.

A laser pulse shape and the output signal of the detector at different times can be generally regarded as a Gaussian shape[22]. Therefore, the small-footprint waveform can be modeled reasonably by a series of Gaussian pulses[23], and several more parameters can be extracted[24]. A return waveform can be decomposed into its Gaussian components in this form:

$$f(x) = b + \sum_{i=1}^{n} a_i e^{-(x-x_i)^2/2\sigma_i^2}, \tag{1}$$

where $f(x)$ represents the received waveform, b is the noise level, and n is the number of Gaussian components. a_i, x_i, and σ_i denote the amplitude, position, and half width (standard deviation) of each Gaussian, respectively. In this letter, a non-linear least-squares method with the Levenberg–Marquardt algorithm[25] was used to decompose the waveforms.

The LiDAR equation (as follows)[24] shows several factors affecting the received echo signal of LiDAR:

$$p_{\mathrm{r}} = \frac{p_{\mathrm{t}} D\mathrm{r}^2}{4\pi R^4 \beta_{\mathrm{t}}^2} \eta_{\mathrm{sys}} \eta_{\mathrm{atm}} \sigma, \tag{2}$$

where p_{r} represents the received power, p_{t} is the transmitted power, $D\mathrm{r}$ is the receiving aperture diameter, R is the range between the sensor and the target, β_{t} is the beam divergence, η_{sys} is a system factor, η_{atm} is an atmospheric transmission factor, and σ is the backscatter cross section. These factors include firing pulse energy, receiver aperture, distance between the target and the aircraft, backscattering cross section or scattering coefficient, attenuation coefficient of a system, and atmosphere. A number of studies have shown that waveform energy and amplitude decrease with the increasing range between the sensor and the target, which is considered to be the most important influential factor of waveform data. In this letter, the LiDAR system of Riegl has the peculiar function of recording transmitted pulses. Several differences have been found by comparing the transmitted pulses. The differences are primarily reflected in energy changes, and the pulse widths are almost the same. Thus, the range between the sensor and the target, as well as the changes in transmitted pulses, are considered during relative calibration, whereas other factors are disregarded as constant because they are difficult to obtain (such as the attenuation coefficient of a system and the atmosphere) or do not change a flight plan (such as the receiver aperture).

A linear proportional relationship between the transmitted pulse energy and the return waveform energy must be assumed to simplify the effect of transmitted pulse energy variations to return echo. Thus, the normalization factor can be described as

$$C_{\mathrm{Index}} = \frac{p_{\mathrm{t\_sta}}}{p_{\mathrm{t}}}, \tag{3}$$

where C_{Index} is the normalization factor, $p_{\mathrm{t\_sta}}$ is the standard transmitted pulse energy, and p_{t} is the transmitted pulse energy. In this letter, $p_{\mathrm{t\_sta}}$ is set as the average of all transmitted pulse energies.

According to the LiDAR equation and the different scattering properties of objects, the relative calibration formula based on the range can be described as (refers to Xu *et al.*[26] for more details regarding the formula derivation)

$$p_{\mathrm{cal}} = p_{\mathrm{r}} \times C_{\mathrm{Index}} \times \left(\frac{R}{R_{\mathrm{cal}}}\right)^n, \tag{4}$$

where p_{cal} is the calibrated energy, p_{r} is the energy of the decomposed Gaussian pulse, R is the range from the sensor to the object, R_{cal} is the reference range, and n is the calibration factor with the values of 2, 3, or 4.

In the correction process, the value of n was varied from 2 to 4 at a step of 0.01. The correlation coefficient of the calibrated values and the corresponding real range was calculated. Then, the value of n at the minimum correlation coefficient was selected as the calibration factor. R_{cal} was set to have the same value of mean range for all flights.

Table 1. Extracted Waveform LiDAR Parameters

Band	Waveform Features of All of the Returns	Band	Waveform Features of the First Return
1	Average Amplitude	6	Average Standard Deviation of First Return
2	Average Energy	7	Average Amplitude of First Return
3	Average Standard Deviation	8	Average Energy of First Return
4	Average Calibrated Amplitude	9	Average Calibrated Amplitude of First Return
5	Average Calibrated Energy	10	Average Calibrated Energy of First Return

Each calibrated amplitude of the Gaussian decomposition result can be computed as

$$a_{i\text{-cal}} = a_i \times C_{\text{Index}} \times \left(\frac{R}{R_{\text{cal}}}\right)^n, \tag{5}$$

where $a_{i\text{-cal}}$ is the calibrated amplitude and a_i is the amplitude of the Gaussian decomposition result.

The Gaussian decomposition results were converted into a multiple-band image while keeping the point cloud information as high as possible. Based on an overall consideration of various objects scales, and the density of LiDAR data collection, an optimum of 4-m^2 pane was introduced to rasterize data, and each grid was assessed using a combination of waveform parameters and other statistical values. These values include the average energy, amplitude, width, calibrated amplitude, and calibrated energy. Then, the classified LiDAR data were transformed into a traditional problem for digital image processing. After the rasterization of the Gaussian decomposition waveform data, six combinations of the three parameter groups were generated. Finally, the 10 most important variables were selected during the preclassification process and listed in Table 1. The 10 parameters were divided into two major categories: parameter mean values of all returns and parameter mean values of the first return. Furthermore, uncalibrated and calibrated data were included in each category.

A supervised method of support vector machines (SVMs), which can account for both spectral information and spatial features[27], was applied to classify LiDAR data. Then, hierarchical classification combined with SVM was implemented to improve classification accuracy. The hierarchical classification method was implemented in two steps. Firstly, the entire image was divided into two major categories, namely, tree and non-tree. Secondly, the tree areas were further divided into needle-leaf and broad-leaf forests, whereas the non-tree areas were further divided into grassland and non-vegetated area using the SVM classifier. In the first step, almost all supervised and unsupervised methods achieve good classification accuracy (over 95%). In the second step, only the band combination of 1, 2, and 3 was adopted in the grassland and non-vegetated area classifications because this combination provides the highest classification accuracy. However, different band combinations (3, 4, and 5; 6, 7, and 8; 6, 9, and 10) were employed in conifer and broad-leaf identification. Regions of interest (ROIs) are defined based on field collection and an exactly matching CCD image. Field data, including single-tree reference information and plot data, were applied in selecting ROIs for conifers and broad-leaf trees. And only the first two crown classes (dominant and codominant) and crown width greater than 4 m of single-tree reference data were considered as reference data. Several ambiguous crown border areas in the aerial image were also neglected. The CCD image was used to select the non-vegetated area and the grassland. Approximately, one-third of the ROIs for each type of land cover had been randomly selected as training data, and the others were defined as the validation set.

The Gaussian decomposition method was applied to the three flight tracks over the study area. The numbers of point clouds and return echoes derived from the Gaussian decomposition are greater compared with those from the real-time echo extraction process of the system. The decomposed waveform data were transformed into 3D points with several related attributes from each decomposed Gaussian waveform, including position, number of target, total number of targets, amplitude, standard deviation, energy, and the range between the sensor and the object.

The gridded image in Fig. 1 reveals subtle differences in the three parameters extracted from the waveform in various feature types. The standard deviation is also referred to in the pulse width of the Gaussian waveform, and it reflects structural differences in the interaction of transmitted pulses with targets. Thus, the pulse width image shows that the width is higher for woody vegetation compared with grass and buildings because trees generally have more complex spatial structures. However, amplitude and energy are lower for trees because of

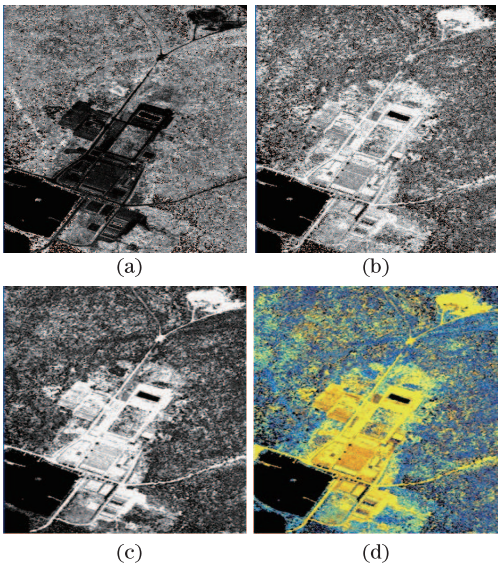

Fig. 1. Parameters extracted from full-waveform data collected over parts of the study area. (a) Average Gaussian standard deviation, (b) mean value of Gaussian amplitude, (c) average Gaussian energy (bright values indicate higher values and low values are dark), and (d) false color composite of a, b and c in RGB color.

the laser energy scattering by multiple layers of trees and lower reflectivity compared with other land-cover types.

Equation (4) was adopted to calibrate the data. The correction factors at the minimum correlation coefficients of the three flight lines are 2.01, 2.03, and 2.08, respectively, which are close to the properties of the extended targets. To assess the calibrated result, the roofs of buildings made from the same material in the study area were selected and used to avoid the effect of different materials in the waveform data. The three strips cover 15, 14, and 9 buildings, respectively. The precalibrated amplitude and energy of the roofs decrease with increasing distance, thus suggesting that precorrected data have a higher relativity with the range than post-calibrated data (Fig. 2). Table 2 indicates that the calibrated data deliver an essentially smaller standard deviation in one flight and that calibrated mean values are closer to each other compared with non-calibrated mean values for different flight paths.

Four combination groups were generated to classify different objects and to evaluate the effect of calibrated and uncalibrated data, first return, and all returns to classification accuracy. Training and validation samples are shown in Table 3. The classification result of the partial trial plot using the hierarchical method is shown in Fig. 3. Overall classification accuracy, kappa coefficient, producer's accuracy, and user's accuracy of the classification results are listed in Table 4. After the comparison of the two classification methods, the total accuracy of the hierarchical classification is determined to be generally better than the corresponding band combination of the normal SVM approach, particularly for tree-species identification, producer's accuracy, and user's accuracy of conifer and broad-leaf trees. Based on Table 4, the classification accuracy of the relative calibrated data increases steadily compared with the uncorrected data. Thus, the improvement of the overall classification accuracy is from 1.2% (comparing 80.52% of the band combination of 1, 2, and 3 with 81.72% of the band combination of 3, 4, and 5 using the normal SVM method) to 6.4% (comparing 79.33% of the band combination of 6, 7, and 8 with 85.77% of the band combination of 6, 9, and 10 using the normal SVM method). Table 4 also shows that the recognition accuracy for grassland and non-vegetated area is superior to that of the tree species, and that the recognition accuracy for broad-leaf trees is the lowest in the four land-cover types.

Table 2. Averages and Standard Deviations of Pre-calibrated and Post-Calibrated Amplitude and Energy

Flight	Amplitude		Energy	
	Pre_c	Post_c	Pre_c	Post_c
1 Mean	24.42	21.23	126.04	113.68
Std	3.30	2.69	11.14	9.29
2 Mean	23.20	21.35	122.13	115.04
Std	3.50	2.01	13.3	11.63
3 Mean	17.97	20.81	106.17	118.42
Std	4.38	2.98	15.2	9.59

Table 3. Training and Validation Samples in Classification

Classes	Grass	Non-vegetation	Conifer	Deciduous
Training Samples	342	267	693	589
Validation Samples	684	533	1 397	1 178
Sum	1 026	800	2 080	1 767

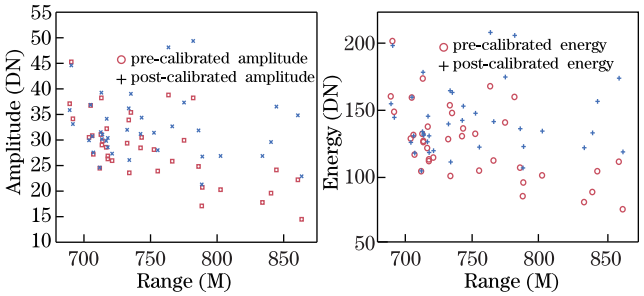

Fig. 2. Profile of pre-calibrated and post-calibrated roofs results with distance.

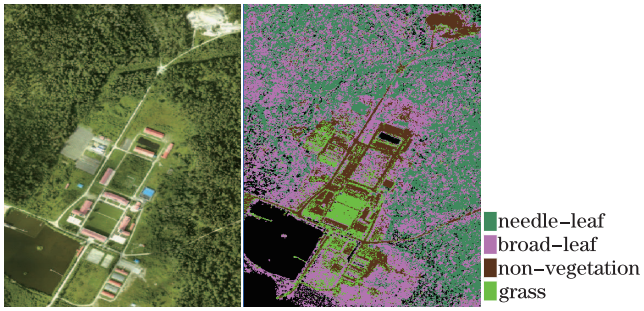

Fig. 3. (a) CCD images of part study area and (b) classification result of hierarchical SVM method with bands of 6, 9, and 10.

This research addresses the effect of relative radiometric correction on the accuracy of classifying land-cover types. A scheme for hierarchical classification usually used in optical remote sensing is also introduced for identifying LiDAR data. This method is an effective means of improving classification accuracy.

Although the calibration approach achieves relatively effective results for object classification, a number of problems are still worthy of further study. Firstly, relative calibration is determined based on the assumption that the surface is a Lambertian reflector without considering the effect of the incidence angle. Moreover, several differences among natural objects are present. The incidence angles of flights 1 and 2 are similar to each other. However, a certain distance exists from flight 3 to the other two flights, and the incidence angles are also different, thus leading to a number of small differences in the calibration results between strips 1, 2, and 3. Therefore, the incidence angle may also be an important factor for calibrating small-footprint waveform data. Secondly, the highest accuracy is found in the band combination with the first return information. This result may be attributed to the first return signal being primarily reflected by the upper-layer information in a footprint and may be better suited in satisfying the requirements of surface classification. However, this process may

Table 4. Classification Accuracy of Different Band Combinations and Methods

Band Class	Normal SVM							
	1-2-3		3-4-5		6-7-8		6-9-10	
	Prod Acc	User Acc	Prod Acc	User Acc	Prod Acc	User Acc	Prod Acc	User Acc
Grass	90.98	93.17	85.88	78.49	89.02	93.03	87.06	92.89
Non-vegetation	98.46	94.40	84.92	96.17	98.77	91.98	98.15	87.64
Needle-Leaf	66.30	78.32	81.64	83.47	66.85	76.73	83.84	84.76
Broad-Leaf	69.97	60.66	75.08	70.15	65.81	59.37	74.12	78.91
Total	Overall Acc = 80.52%		Overall Acc = 81.72%		Overall Acc = 79.33%		Overall Acc = 85.77%	
	Kappa Coe = 0.7395		Kappa Coe = 0.7554		Kappa Coe = 0.7233		Kappa Coe = 0.8091	
Band Class	Hierarchical SVM							
	1-2-3		3-4-5		6-7-8		6-9-10	
	Prod Acc	User Acc	Prod Acc	User Acc	Prod Acc	User Acc	Prod Acc	User Acc
Grass	96.08	90.07	96.08	90.07	96.08	90.07	96.08	90.07
Non-vegetation	99.38	92.02	99.38	92.02	99.38	92.02	99.38	92.02
Needle-Leaf	78.71	77.25	84.66	85.83	78.08	74.61	87.40	84.62
Broad-Leaf	67.89	72.76	70.93	80.73	56.23	69.57	72.69	83.33
Total	Overall Acc = 82.18%		Overall Acc = 87.36%		Overall Acc = 81.80%		Overall Acc = 87.6%	
	Kappa Coe = 0.7622		Kappa Coe = 0.8307		Kappa Coe = 0.7560		Kappa Coe = 0.8338	

cause the misclassification phenomenon of non-first-return points and may not fundamentally address the effect of multiple echoes to the return waveform. Enhancing the comparability of multiple echoes and single echo requires an in-depth mechanistic research on LiDAR. That is, current waveform data correction theory is not perfect, and a unified standard has not been developed yet.

A 4-m^2 pane is introduced to raster the data, thus leading to a surface classification result. The grid classification results can construct point cloud types and reduce the degree of fragmentation; however, a misclassification phenomenon may occur in several areas. Meanwhile, the last return (as the presumed ground) is not involved in calculating grid value. These issues should be addressed in the process of transforming grid classification into point cloud types in future research.

The overall results show that the parameters acquired from waveform can distinguish grassland, non-vegetated area, needle-leaf trees, and broad-leaf trees without elevation or geometric information. The following important aspects can be concluded.

Compared with point ground data from the system, waveform Gaussian decomposition increases spatial point density and provides additional attributes for the detected points.

Calibrating full-waveform data is necessary before they can be applied in object classification. The parameters of the groups of corrected data improve classification accuracy by an additional 1.2% to 6.4% compared with uncalibrated data. Such improvement is primarily reflected in identifying needle-leaf and broad-leaf trees, which will promote the use of waveform data in forestry applications.

The layered classification method is useful in reforming classification accuracy. This result is primarily attributed to the fact that the three studied parameters are clearly different for forest and non-forest areas. Therefore, the total accuracy for adopting any supervised or unsupervised method can reach 95% to 98%, thus effectively avoiding confusion between these two categories.

This work was supported by the National "863" Program of China (No. 2012AA12A306) and the National Natural Science Foundation of China (No. 41071272).

References

1. B. Petzold, P. Reiss, and W. Stössel, ISPRS J. Photogramm. Remote Sensing **54,** 95 (1999).
2. S. O. Elberink and H. G. Mass, International Archives of the Photogrammetry, Remote Sensing and Spatial Information Sciences **33,** 678 (2000).
3. T. Melzer, J. Appl. Geodesy **1,** 159 (2007).
4. J. Shen, J. Liu, X. Lin, and R. Zhao, Sensor Lett. **10,** 221 (2012).
5. D. S. Lee and J. Shan, Marine Geodesy **26,** 117 (2003).
6. A. Persson, J. Holmgren, U. Sodermann, and H. Olsson, in *Proceedings of the ISPRS Working Group VIII/2, Laser-Scanners for Forest and Landscape Assessments*10-03 (2004).
7. E. Puttonen, J. Anttoni, L. Paula, and H. Juha, Sensors **11,** 5158 (2011).
8. W. Wagner, M. Hollaus, C. Briese, and V. Ducic, Int. J. Remote Sens. **29,** 1433 (2008).
9. A. Persson, U. Söderman, and S. Ahlberg, International

Archives of Photogrammetry, Remote Sensing and Spatial Information Sciences **36,** 103 (2005).
10. C. Briese, H. Bernhard, L. Hubert, W. Wagner, P. Martin, and U. Andreas, Proc. SPIE **6950,** 69500H (2008).
11. M. Doneus and C. Briese, in *Proceedings of The 7th International Symposium on Virtual Reality, Archaeology and Cultural Heritage VAST* 155 (2006).
12. C. Mallet and F. Bretar, ISPRS J. Photogramm. Remote Sens. **64,** 1 (2009).
13. J. Reitberger, P. Krzystek, and U. Stilla, International Archives of Photogrammetry, Remote Sensing and Spatial Information Sciences **36,** 332 (2007).
14. J. Reitberger, P. Krzystek, and U. Stilla, Int. J. Remote Sens. **29,** 1407 (2008).
15. A. L. Neuenschwander, L. A. Magruder, and M. Tyler, J. Appl. Remote Sens. **3,** 033544 (2009).
16. B. Höfle, M. Hollaus, H. Lehner, N. Pfeifer, and W. Wagner, SilviLaser 227 (2008).
17. W. Wagner, ISPRS J. Photogramm. Remote Sens. **65,** 505 (2010).
18. A. Kukko, S. Kaasalainen, and P. Litkey, Appl. Opt. **47,** 986 (2007).
19. B. Hofle and N. Pfeifer, ISPRS J. Photogramm. Remote Sens. **62,** 415 (2007).
20. S. Kaasalainen, J. Hyyppä, P. Litkey, and H. Hyyppä, ISPRS J. Photogramm. Remote Sens. **36,** 201 (2007).
21. A. Vain, S. Kaasalainen, P. Ulla, K. Anssi, and L. Paula, Sensors **9,** 2780 (2009).
22. L. Wu, Y. Zhang, L. Cao, N. Zhao, J. Wu, and Y. Zhao, Chin. Opt. Lett. **10,** 122802 (2012).
23. M. A. Hofton, J. B. Minster, and J. B. Blair, IEEE Trans. Geosci. Rem. Sens. **38,** 1989 (2000).
24. W. Wagner, A. Ullrich, V. Ducic, T. Melzer, and N. Studnicka, ISPRS J. Photogramm. Remote Sens. **60,** 100 (2006).
25. M. Craid, "Curve Fitting and Function Optimization", http://cow.physics.wisc.edu/∼craigm//idl/fitting.html (Jan 31, 2013).
26. G. Xu, Y. Pang, and Z. Li, Proc. SPIE **8286,** 82860V (2011).
27. K. Tan and P. Du, Chin. Opt. Lett. **9,** 011003 (2011).